

# Journal of Materials Chemistry A

Accepted Manuscript



This is an *Accepted Manuscript*, which has been through the Royal Society of Chemistry peer review process and has been accepted for publication.

*Accepted Manuscripts* are published online shortly after acceptance, before technical editing, formatting and proof reading. Using this free service, authors can make their results available to the community, in citable form, before we publish the edited article. We will replace this *Accepted Manuscript* with the edited and formatted *Advance Article* as soon as it is available.

You can find more information about *Accepted Manuscripts* in the [Information for Authors](#).

Please note that technical editing may introduce minor changes to the text and/or graphics, which may alter content. The journal's standard [Terms & Conditions](#) and the [Ethical guidelines](#) still apply. In no event shall the Royal Society of Chemistry be held responsible for any errors or omissions in this *Accepted Manuscript* or any consequences arising from the use of any information it contains.

# Hysteresis-free and highly stable perovskite solar cells produced via a chlorine-mediated interdiffusion method

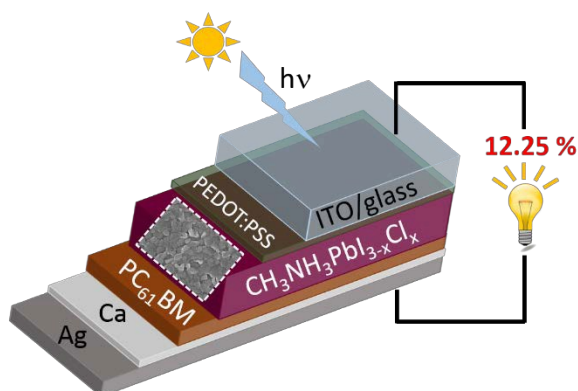
Neeti Tripathi,<sup>a</sup> Masatoshi Yanagida,<sup>ab</sup> Yasuhiro Shirai,<sup>\*ab</sup> Takuya Masuda,<sup>a</sup> Liyuan Han,<sup>b</sup> and Kenjiro Miyano<sup>a</sup>

<sup>a</sup> Global Research Center for Environment and Energy based on Nanomaterials Science (GREEN), National Institute for Materials Science (NIMS), 1-1 Namiki, Tsukuba, Ibaraki 305-0044, Japan. \*E-mail: shirai.yasuhiro@nims.go.jp

<sup>b</sup> Photovoltaic Materials Unit, National Institute for Materials Science (NIMS), 1-2-1 Sengen, Tsukuba, Ibaraki 305-0047, Japan

## Table of contents entry

Perovskite solar cells fabricated using chlorine-mediated interdiffusion method showed promising stability over 2 months with encapsulation and no immediate degradation under continuous light exposure.



## Abstract

Although lead-halide perovskite-based solar cells hold the promise of a breakthrough in the production of next-generation photovoltaic devices, anomalous hysteresis in current-voltage curves and inadequate stability remain as major challenges. Here, we demonstrate the production of low-temperature solution-processed perovskite solar cells (ITO/PEDOT:PSS/perovskite/PC<sub>61</sub>BM/Ca/Ag) with hysteresis-free current-voltage characteristics, excellent photostability, and high reproducibility via the inclusion of methyl ammonium chloride (MACl) using the interdiffusion method. The best-performing devices exhibited a power conversion efficiency of over 12%. Our devices showed promising stability by maintaining more than 90% of their initial performance over long periods of time at ambient conditions with encapsulation using common techniques, as well as no obvious degradation after 2 h of continuous light exposure. We statistically compared fabrication

processes using the interdiffusion method with or without MACl by creating a histogram of over 120 devices for each method. The results clearly indicated that including MACl gave better reproducibility and a higher average efficiency of 9.5%, as well as improved device stabilities.

## Introduction

Organic/inorganic hybrid solar cells based on metal-halide perovskite are considered promising candidates for third-generation photovoltaics because of their efficient photovoltaic performance, simple processing conditions, and comparatively low cost.<sup>1-7</sup> Kojima *et al.*<sup>2</sup> published the first report of a perovskite-based dye-sensitized solar cell with a power conversion efficiency (PCE) of 3.8%, but rapid progress in this area in the last 5 years has now increased the PCE to more than 15%.<sup>3-8</sup> Initially, state-of-the-art perovskite-based devices used a metal-oxide porous scaffold (TiO<sub>2</sub>, Al<sub>2</sub>O<sub>3</sub>, and ZnO).<sup>4, 6, 9, 10</sup> However, in later reports, device processing was simplified by using a planar configuration to avoid the crucial penetration of perovskite into the porous layers.<sup>3, 7</sup> To date, different deposition techniques, such as single step<sup>11</sup> two-step<sup>4</sup>, and vapor deposition<sup>3</sup> methods, have been employed to fabricate these devices. Nevertheless, the use of oxide materials as electron-selective layers generally requires high-temperature processing.

Another direction of growing research into perovskite solar devices involves low-temperature solution-processable electron- and hole-transport materials, which have been commonly used in organic photovoltaics (OPVs).<sup>5, 12-15</sup> The first work on a perovskite solar cell with structures similar to the OPV devices was reported by Jeng *et al.*,<sup>12</sup> using [poly(3,4-ethylenedioxythiophene):poly-(styrenesulfonic acid)] (PEDOT:PSS) as a hole-transporting layer and phenyl-C<sub>61</sub>-butyric acid methyl ester (PC<sub>61</sub>BM) as an electron-selective layer in planar heterojunction configuration. However, PCE was limited to 3.9% owing to the difficulty in forming the uniform perovskite films on top of the PEDOT:PSS layer. Later, Docampo *et al.*<sup>13</sup> demonstrated improved PCE (up to 10%) by using an inverted device structure on fluorine-doped tin oxide (FTO); they speculated that the smooth surface of the indium tin oxide (ITO) substrate was unfavorable for uniform spreading of the perovskite layer. Nevertheless, advancements in the development of ITO-based devices achieved efficiencies of over 15% by using the interdiffusion process developed by Xiao *et al.*,<sup>5</sup> which, unlike the sequential dipping method, provides a homogenous layer of perovskite for planar devices. Another report by Chiang *et al.* on the interdiffusion method<sup>16</sup> demonstrated

efficiencies of up to 16.31%; this enhancement in efficiency was attributed to the better electron mobility of PC<sub>71</sub>BM compared with that of PC<sub>61</sub>BM.

Since the development of perovskite photovoltaic devices, a huge amount of attention has been paid to increasing their efficiency. However, inadequate stability remains a central challenge to the adoption of perovskite photovoltaics. Producing hysteresis-free devices with sustainable performance seems to be essential for future progress in the development of perovskite solar cells. Devices with hysteresis behaviors in J-V responses show a large discrepancy between the forward and reverse scans, resulting in considerable errors in evaluating the solar cell efficiencies.<sup>7, 17, 18</sup> For example, the results reported by Zhou *et al.*<sup>7</sup> showed a large degree of hysteresis in device performance (16.79% efficiency in reverse scan and 13.08% in forward scan), and device performance deteriorated after a very short time.

A study by Kim and Park<sup>19</sup> showed that the degree of hysteresis depends strongly on the perovskite crystal size and the presence of the mesoporous layer. Very recently, Unger *et al.*<sup>20</sup> presented a detailed study of the hysteresis effect and suggested that the transient behavior of perovskite photovoltaic devices can be influenced by the stoichiometry of the perovskite material, as well as by the degree of crystallinity and the size of the crystalline domains. Although a wide number of fabrication methods<sup>4-6, 11</sup> have been investigated, it is difficult to find one optimized method that can ensure both high quality of the perovskite absorber without anomalous hysteresis behavior and unperturbed device performance with long-term stability.

Here, we demonstrate solar devices that were prepared by using a low-temperature-resolution process and have hysteresis-free current–voltage characteristics and excellent long-term stability. Our devices show promising stability by maintaining more than 90% of their initial performance over a long period of time at ambient conditions when encapsulated by using a common method. Indeed, this degree of device stabilities allowed us to quantitatively analyze the perovskite photovoltaic cells by using analytical models and impedance spectroscopy (IS); the J-V measurements were perfectly consistent with a simple diode model, and the IS in darkness and under illumination revealed a very slow process reminiscent of hopping conduction.<sup>21</sup> In this study, we compared the photovoltaic properties and stability of two different lead-halide perovskite devices (i.e. MAPbI<sub>3</sub> and MAPbI<sub>3-x</sub>Cl<sub>x</sub>) fabricated by using the interdiffusion method.<sup>5, 16</sup> Many studies have used mixed iodide/chloride in the perovskite film formation to improve film qualities, and the role of the chlorine has been a topic of much debate.<sup>22-25</sup> We found that improved film morphology could be achieved by adding a small amount of methyl ammonium chloride (MACl) to the methyl ammonium

iodide (MAI) solution in the interdiffusion process to produce Cl-doped  $\text{MAPbI}_{3-x}\text{Cl}_x$  devices instead of  $\text{MAPbI}_3$  ones. This combination of a doping approach with the interdiffusion method yields smoother perovskite films that have greater reproducibility and photostability. By employing this method, we found that the best-performing device had a PCE of 12.3% (device area  $0.08 \text{ cm}^2$ ). A statistical study of the fabrication of more than 240 devices with and without MAI unambiguously revealed the advantage of Cl-doped  $\text{MAPbI}_{3-x}\text{Cl}_x$  devices. We also report our detailed analysis of the hysteresis-free behaviors of our devices, as evaluated by using hysteresis index approaches, and the results of stability testing under continuous light exposure (1 sun) for 2 h and in ambient conditions over 2 months.

## Experimental section

### Materials and characterization

All chemicals were purchased from commercial suppliers and used as received unless stated otherwise.  $\text{PbI}_2$  (Sigma Aldrich, 99%) and methyl ammonium iodide (MAI) (Wako Chem., 98%) were dissolved in anhydrous N, N-dimethylformamide (Wako chem., 99.5%)( $400 \text{ mg}\cdot\text{ml}^{-1}$ ) and anhydrous 2-propanol (Wako chem.)( $50 \text{ mg}\cdot\text{ml}^{-1}$ ), respectively. For chlorine doping, 5-20 wt% MAI (Wako chem.) was mixed with the MAI solution.  $\text{PC}_{61}\text{BM}$  (Solenne or Lumitec, 99%) solution (2 wt%) dissolved in anhydrous chlorobenzene (Wako chem., 99%) was used for coating of the electron selective layer. All the solutions were filtered using  $0.45 \mu\text{m}$  syringe filters to avoid the risk of particle formation. UV-curable resins (NagaseChemtex XNR5516Z) were used to seal devices with cavity glasses. The x-ray diffraction patterns of  $\text{MAPbI}_3$  and  $\text{MAPbI}_{3-x}\text{Cl}_x$  were collected using Bruker D8 advanced x-ray diffractometer ( $\text{CuK}\alpha$  radiation,  $\lambda = 1.54050 \text{ \AA}$ ). The top surface and cross-sectional images were taken by a high resolution scanning electron microscope at 5 kV accelerating voltage (Hitachi-4800). Additionally, elemental mapping was done using energy dispersive x-ray measurement mode at accelerating voltage of 10 kV. The current density–voltage (J-V) characteristics under 1 sun with an AM 1.5G spectral filter ( $100 \text{ mW}/\text{cm}^2$ , calibrated with a Si reference cell, emission spectrum in Figure S9) and incident monochromatic photon to current conversion efficiency (IPCE) spectra or External quantum efficiency (EQE) were measured with a CEP-200BX spectrometer (Bunkoeki, Tokyo, Japan) at room temperature. To investigate the hysteresis behaviour scan rates were varied from 0.02 to 0.3 V/s. Histogram of over 240 devices were generated from the devices using  $0.18 \text{ cm}^2$  aperture mask.

## Device fabrication

Solar cell devices were fabricated on pre-cleaned patterned indium tin oxide (ITO) coated glass substrates ( $15 \Omega \text{ square}^{-1}$ ). The ITO substrates were pre-cleaned in an ultrasonic bath with detergent, pure water, and 2-propanol, and then treated in an ultraviolet-ozone chamber for at least 10 min to remove the organic residuals. A thin layer ( $\sim 30 \text{ nm}$ ) of PEDOT:PSS (Clevios, AI4083) was formed by spin coating at 3000 rpm and subsequently dried at  $140^\circ\text{C}$  for 10 min on a hot plate under air. Substrates were transferred into a nitrogen-filled glove box ( $<1.0 \text{ ppm O}_2$  and  $\text{H}_2\text{O}$ ) for  $\text{PbI}_2$  and MAI coatings. Firstly,  $\text{PbI}_2$  was spin coated on to the top of PEDOT:PSS layer at 3000 rpm for about 30 sec. After drying at  $70^\circ\text{C}$  for 30 min, MAI solutions with different MAI weight percentages were spun on to the  $\text{PbI}_2$  layer at 4000 rpm, 30 sec. These  $\text{PbI}_2/\text{MAI}$  samples were heated at  $100^\circ\text{C}$  for 2 hours for the complete conversion into perovskite. Finally, a  $\text{PC}_{61}\text{BM}$  layer was spun on the perovskite layer at 700 rpm for 60 s. Samples were then transferred into the evaporation chamber, connected to the glove box for metal contact deposition. A 4 nm thin layer of Ca and 100 nm of Ag were deposited by thermal evaporation at a pressure  $<10^{-4} \text{ Pa}$ . This process provided devices with  $4.0 \times 7.5 \text{ mm}^2$ , and they are sealed using the UV-curable resin before the subsequent measurements in ambient conditions with an aperture mask of  $0.08$  to  $0.18 \text{ cm}^2$ .

## Results and discussion

Figure 1 is a simplified energy-band diagram of the solar cells used in this work. The perovskite layer was deposited by using the interdiffusion method, and then the  $\text{PC}_{61}\text{BM}$  layer was deposited via a spin-coating method, instead of the vacuum evaporation technique used previously,<sup>5</sup> thus a more attractive solution-based fabrication process was used. An ultra-thin layer of calcium (Ca) in conjugation with silver (Ag) was evaporated as the back contact to complete the device structure. The combination of low-work-function Ca and Ag was used to obtain better ohmic contacts at the cathode interface.<sup>26</sup>

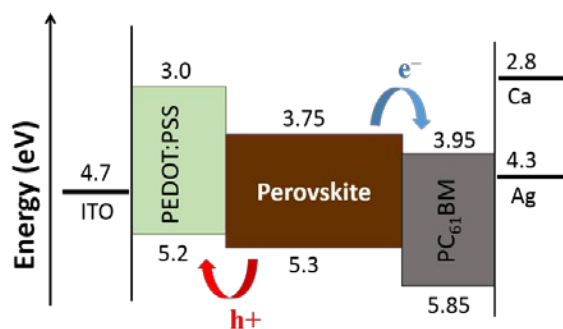


**Figure 1.** Simplified energy-band diagram of the low-temperature solution–deposited planar perovskite solar cell device.

To investigate the structural evolution of the device, XRD patterns of MAPbI<sub>3</sub> and MAPbI<sub>3-x</sub>Cl<sub>x</sub> films were recorded before annealing and after 10 min and 2 h of annealing at 100 °C (Fig. 2). For comparison, all the diffraction patterns were plotted at the same intensity scale. The main diffraction peaks at 2 θ positions 14.04° and 28.42° were assigned to the (110) and (220) diffraction planes of MAPbI<sub>3</sub>,<sup>3, 12, 27</sup> whereas the broad hump at about 20° corresponded to the ITO/glass substrate. Interestingly, before annealing, MAPbI<sub>3</sub> films had almost negligible features, whereas a prominent peak corresponding to the (220) plane of the tetragonal perovskite structure was clearly apparent in the case of MAPbI<sub>3-x</sub>Cl<sub>x</sub> films. Before the annealing, the presence of a small peak of PbI<sub>2</sub> on both films suggested incomplete reactions. After annealing at 100 °C for 10 min, samples of both MAPbI<sub>3</sub> and MAPbI<sub>3-x</sub>Cl<sub>x</sub> gave identical XRD patterns, although the patterns differed slightly in intensity scale. When we increased the annealing time to 2 h there was no further improvement in the case of the MAPbI<sub>3</sub> film, whereas the XRD pattern of the MAPbI<sub>3-x</sub>Cl<sub>x</sub> film showed a marked increase in intensity of the (110) and (220) planes.

The increase in the intensity ratio of the (110) to (220) planes in the case of MAPbI<sub>3-x</sub>Cl<sub>x</sub>—from 2.25 to 2.62—after 2 h of annealing is a possible indication of chlorine ion–assisted slow growth along the preferred (110) orientation. The crystallite sizes (L) of the MAPbI<sub>3</sub> and MAPbI<sub>3-x</sub>Cl<sub>x</sub> films were estimated by using the Scherrer formula,<sup>28</sup> given by  $L = (0.9\lambda)/(\beta \cos\theta)$ , where  $\lambda = 0.154$  nm for CuK $\alpha$  radiation and  $\beta$  is the full width at half maximum of the diffraction peak, in radians. Crystallite sizes for MAPbI<sub>3-x</sub>Cl<sub>x</sub> (95 nm) were greater than those MAPbI<sub>3</sub> (70 nm).

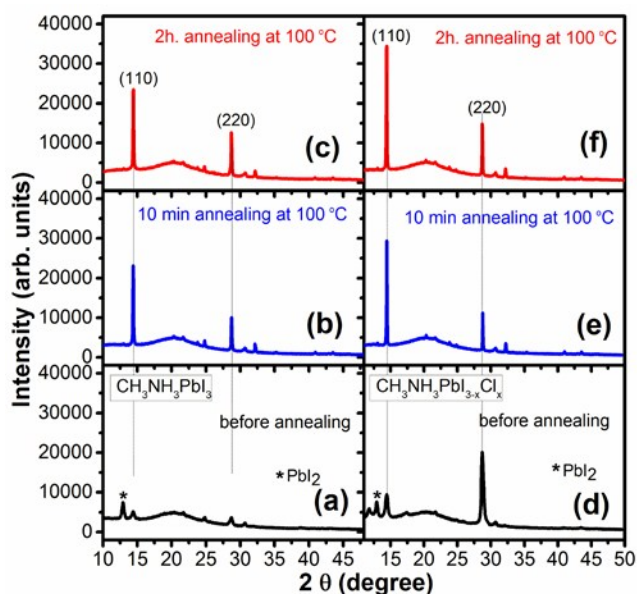


**Figure 2.** XRD patterns of perovskite films before annealing and after annealing for different periods of time: (a) to (c), MAPbI<sub>3</sub>; (d) to (f), MAPbI<sub>3-x</sub>Cl<sub>x</sub>.

These different evolutions of the XRD patterns of the MAPbI<sub>3</sub> and MAPbI<sub>3-x</sub>Cl<sub>x</sub> films suggested that there were two distinct reaction-crystallization processes. In the case of MAPbI<sub>3</sub>, the reaction was barely initiated before annealing, whereas within 10 min of the start of annealing the reaction crystallization had proceeded rapidly and was complete, with no further changes between then and 2 h. On the other hand, in the case of MAPbI<sub>3-x</sub>Cl<sub>x</sub>, the reaction started before annealing, but after the initial reaction the process slowed and completed within 2 h. For the one-step coating process with PbCl<sub>2</sub> and MAI on PEDOT:PSS surfaces, the existence of chlorine has shown a striking effect on the microstructure and orientation of perovskite films through the templated topotactic self-assemblies.<sup>23</sup> Although large differences can be expected between the one-step method and the interdiffusion method employed in this study, the presence of chlorine can effectively alter the course of crystallization processes and may improve the orientational order and degree of crystallinity. The increased crystal size in MAPbI<sub>3-x</sub>Cl<sub>x</sub> can reduce charge trapping and recombination at grain boundaries, thereby improving the fill factor (FF) owing to better film formation and hence a reduction in the number of shunting paths.<sup>29</sup> Noticeably, the absence of any intermediate impurity phases even before annealing suggests that a chlorine-assisted interdiffusion method is capable of producing high-quality MAPbI<sub>3</sub>Cl<sub>3-x</sub> films. Another point is that continuous and smooth perovskite films were obtained on the crystalline PbI<sub>2</sub> films (Figure S1). Therefore, the extra effort of preparing an amorphous or conformal PbI<sub>2</sub> layer,

which generally requires the  $\text{PbI}_2$  solution or ITO substrate, or both, to be heated during the deposition process,<sup>5</sup> can be avoided by using this method.

We carefully inspected the morphological changes in the  $\text{MAPbI}_3$  and  $\text{MAPbI}_{3-x}\text{Cl}_x$  perovskite films by using scanning electron microscopy (SEM) before and after  $\text{PC}_{61}\text{BM}$  coating (Figure 3). Top and cross-sectional views of the  $\text{MAPbI}_3$  layer without the  $\text{PC}_{61}\text{BM}$  coating are shown in Figure 3 (a) and (b), respectively. Large variations in crystallite size with islands of sub-micron size can be seen clearly all over the surface (Figure 3 (a)). Although the average thickness of the perovskite layer seems to be uniform, the presence of these random structures on the surface (marked by circles, Figure 3 (b)) increases the possibility of current leakage occurring through piercing of the thin  $\text{PC}_{61}\text{BM}$  layer to the cathode. In contrast, we were able to produce very smooth, continuous, and pin-hole-free perovskite films by using the interdiffusion method with a mixture of both  $\text{MACl}$  and  $\text{MAI}$ , as seen in the top and cross-sectional views (Figure 3 (c) and (d), respectively). It was possible that the rough features on top of the perovskite layer could be smoothed by being covered with the slightly thicker  $\text{PC}_{61}\text{BM}$  layer. However, this was not the case with  $\text{MAPbI}_3$ , as the sharp features on the perovskite surface were still visible even after the addition of a 70-nm-thick  $\text{PC}_{61}\text{BM}$  layer (Figure 3 (e)). As expected,  $\text{MAPbI}_{3-x}\text{Cl}_x$  gave smooth films both before and after  $\text{PC}_{61}\text{BM}$  coating (Figure 3 (f)). These random morphological and crystallite size features can affect the device's performance. By performing electron beam-induced current profiling, Edri *et al.*<sup>30</sup> found a uniform current distribution throughout  $\text{MAPbI}_{3-x}\text{Cl}_x$ -based solar cells but a grain-dependent current distribution in  $\text{MAPbI}_3$  cells. The enhanced  $J_{\text{sc}}$  value of  $\text{MAPbI}_{3-x}\text{Cl}_x$  that we found here was in good agreement with these previous observations.

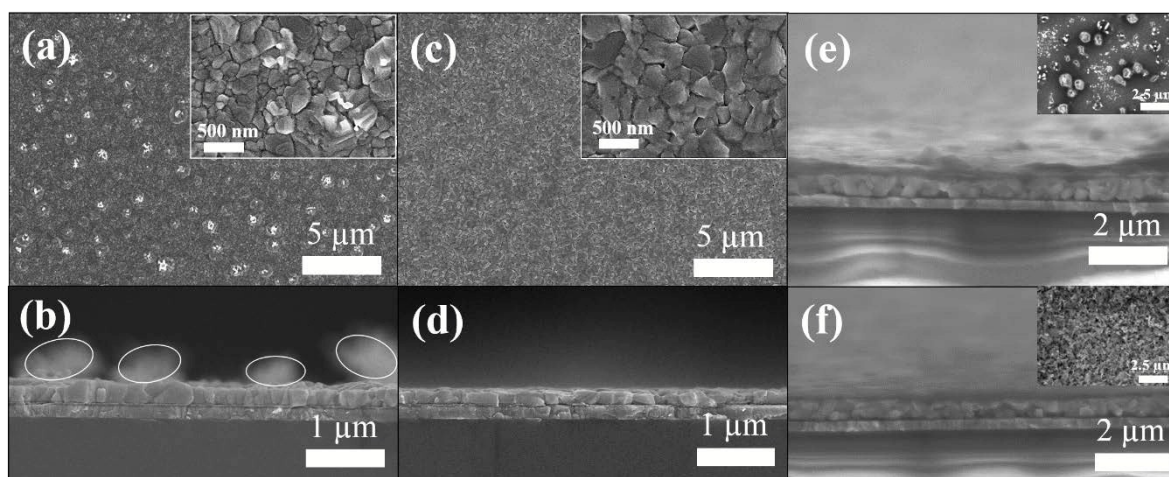


**Figure 3.** SEM images (a) and (b): top and cross-sectional views of MAPbI<sub>3</sub> without PC<sub>61</sub>BM coating; (c) and (d): top and cross-sectional views of MAPbI<sub>3-x</sub>Cl<sub>x</sub> without PC<sub>61</sub>BM coating; (e) cross-sectional view of sample MAPbI<sub>3</sub> with PC<sub>61</sub>BM coating [inset shows top view]; (f) cross-sectional view of MAPbI<sub>3-x</sub>Cl<sub>x</sub> with PC<sub>61</sub>BM coating [inset shows top view].

Solution-processed perovskite solar cells are highly sensitive to crystallization conditions such as the choice of precursors, concentrations, solvents, annealing temperatures, and annealing times. A small variation in structural and morphological properties can lead to a huge step-down in device performance. In our experience, without the MAI, it was difficult to obtain better control of film formation even though the synthesis process was optimized by adjusting several parameters such as the precursor concentration, spin speed, solution dispensing method (static or dynamic dispensing of spin coatings), and annealing temperature or duration (or both). Although comparable PCEs were achieved in some attempts, the reproducibility of the MAPbI<sub>3</sub> devices was poorer than that of the Cl-doped MAPbI<sub>3-x</sub>Cl<sub>x</sub> devices. The Cl-doped perovskite films showed consistently improved crystalline structure and morphology, irrespective of small variations in PbI<sub>2</sub> or MAI concentrations and spin-coating methods. A cross-sectional view of a MAPbI<sub>3-x</sub>Cl<sub>x</sub> film, with the estimated thickness of each layer, is shown in Figure 4 (a). The thicknesses of the PEDOT:PSS, MAPbI<sub>3-x</sub>Cl<sub>x</sub>, and PC<sub>61</sub>BM layers were ~30 nm, ~245 nm, and ~70 nm, respectively.

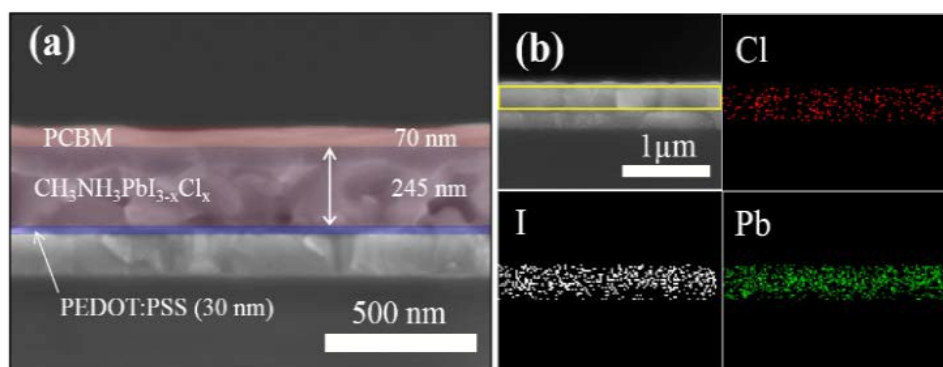


**Figure 4.** (a) Cross-sectional view and (b) elemental mapping of MAPbI<sub>3-x</sub>Cl<sub>x</sub>.

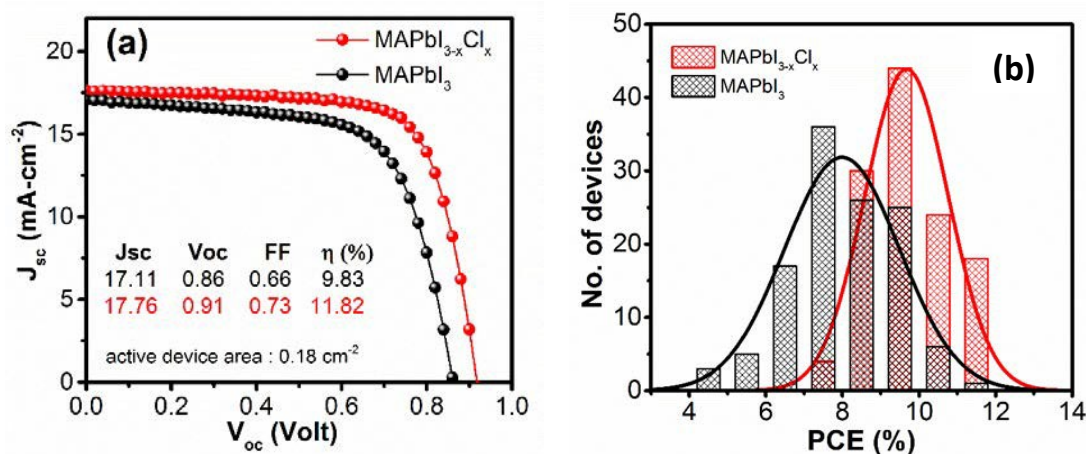
We also evaluated the amounts of chlorine atoms left in the MAPbI<sub>3-x</sub>Cl<sub>x</sub> films by measuring the ratio of chlorine to iodine using x-ray photoemission spectroscopy (XPS). The amount of chlorine, however, seemed to be below the sensitivity limit of the instrument. We

also conducted a XPS depth-profiling analysis by etching the film surface step by step up to a depth of ~50 nm (Figure S2); a small hump was observed at the Cl-2p core level position. Although the inherently weak signal from chlorine compared with that of iodine meant that we had insufficient reliable information, we concluded that the chlorine content of the bulk film was likely of the order of 1% and that, on the basis of the depth profiles, the chlorine was not segregated on the surface. Considering the results of other studies, however, it seemed reasonable to have such low chlorine concentrations in our devices because only small amounts of chlorine (in the range of 2% to 4%) have been detected, even in films prepared from precursors with much greater chlorine contents (MAI:PbCl<sub>2</sub>, 3:1).<sup>31, 32</sup> Furthermore, we made another attempt at elemental mapping by using energy-dispersive x-ray (EDX) measurement (Figure 4 (b)). Traces of chlorine signals were observed in the MAI-doped samples, and the chlorine signal consistently increased with increasing MAI concentration in the MAI solution (Supplementary information Table S1). Note that only qualitative information can be obtained from EDX analyses. Nevertheless, it was clear that the amount of chlorine incorporated into the perovskite structure was far less than the nominal composition of up to 20% MAI mixed in the MAI solution that was spread on the surface. Indeed, recent studies clearly revealed sublimation and loss of chlorine contents under mild annealing conditions below 100 °C.<sup>22</sup>

In response to the very different XRD results for the non-annealed MAPbI<sub>3</sub> and MAPbI<sub>3-x</sub>Cl<sub>x</sub> films (see Figure 2 and the discussions thereafter), we compared the morphologies of MAPbI<sub>3</sub> and MAPbI<sub>3-x</sub>Cl<sub>x</sub> before annealing (Figure S3). MAPbI<sub>3</sub> perovskite films have a very rough surface and non-uniform thickness, possibly because of the presence of unreacted MAI or PbI<sub>2</sub> on the surface. In contrast, the highly compact and smooth nature of the layer in the Cl-doped perovskite films implied that adding a small amount of MAI to the MAI solution had a huge impact on the structure and morphology of the non-annealed perovskite layer. SEM comparison of the features of PbI<sub>2</sub>, PbI<sub>2</sub>/MAPbI<sub>3</sub>, and PbI<sub>2</sub>/MAPbI<sub>3-x</sub>Cl<sub>x</sub> films revealed the formation of a continuous film with a morphology resembling that of the underneath PbI<sub>2</sub> layer in the case of Cl-doped perovskite (Figure S4); this was in contrast to the morphology of the MAPbI<sub>3</sub> perovskite film, with its sub-micron-size random features.

It is well known that the crystallinity and morphology of the perovskite layer determine the ultimate performance of the device, as non-uniformity causes current leakage and defects cause the development of trapping sites for charge recombination. Figure 5(a) shows the J-V curves for MAPbI<sub>3</sub> and MAPbI<sub>3-x</sub>Cl<sub>x</sub> devices (device size, 0.18 cm<sup>2</sup>) prepared

in the same batch. We observed a clear correlation between morphology and the device parameters, as evident from the substantial improvement in photovoltaic parameters in MAPbI<sub>3-x</sub>Cl<sub>x</sub> devices. Both interdiffusion methods—with or without the chlorine doping—worked well, and in both cases the PCEs reached almost 12% in our hands. These results paralleled those of original reports on the interdiffusion method using vapor-deposited fullerenes (PCE 15.4%) or spin-coated PC<sub>61</sub>BM (PCE 9.92%).<sup>16</sup> However, we found that, generally, devices prepared by using the Cl-doped interdiffusion method had better performances. We obtained statistical insight into the process of fabrication using the MAPbI<sub>3-x</sub>Cl<sub>x</sub> and MAPbI<sub>3</sub> films by creating a histogram of the PCEs of 120 devices for each film type (Figure 5(b)). The results clearly indicated that the MAPbI<sub>3-x</sub>Cl<sub>x</sub> devices gave better reproducibility, with a higher average efficiency of 9.5%, whereas the MAPbI<sub>3</sub> devices had a broad and lower distribution of efficiencies. Furthermore, detailed analysis of the J-V curves for each device revealed, as a general trend, a decrease in series resistance and an increase in shunt resistance in the case of the MAPbI<sub>3-x</sub>Cl<sub>x</sub> devices. As a result, a marked improvement in FF was observed in the case of MAPbI<sub>3-x</sub>Cl<sub>x</sub> devices; this was ascribable to the relatively small number of grain boundaries and lack of leakage paths in the homogenous perovskite films. The improvement in FF could also be related to the high carrier mobility of chlorine-doped devices.<sup>1,33</sup> The IPCE spectra for the devices were also compared (Figure 5 (c)). MAPbI<sub>3-x</sub>Cl<sub>x</sub> devices had IPCEs slightly superior to those of MAPbI<sub>3</sub> devices. The IPCE peaked at about 75% at wavelengths of 430 to 540 nm and 670 nm, consistent with other reports.<sup>33,34</sup> Integrated J<sub>sc</sub> values of 16.90 and 17.58 mA cm<sup>-2</sup> were obtained for MAPbI<sub>3-x</sub>Cl<sub>x</sub> and MAPbI<sub>3</sub>, respectively; these were in good agreement with the photocurrent densities obtained from the J-V curves.



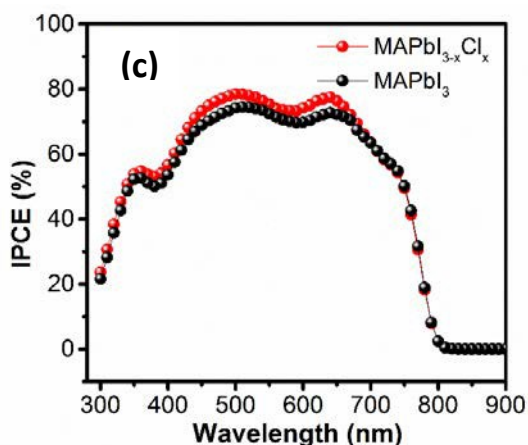


**Figure 5.** (a) J-V characteristics prepared in the same batch and (b) Efficiency histogram of 120 devices for each method [device size  $0.18 \text{ cm}^2$ ] (c) IPCE spectra of  $\text{MAPbI}_3$  and  $\text{MAPbI}_{3-x}\text{Cl}_x$  devices prepared in the same batch.

We also verified the dependence of PCE on perovskite device size. It is generally more convenient (but less reliable) to achieve higher efficiency in smaller devices, as one can better avoid defects or pinholes using smaller devices, which also have fewer conductivity problems than with the larger transparent electrodes in larger devices. However, there are more errors in the smaller apertures used with smaller devices. To compare our devices ( $0.18 \text{ cm}^2$ ) with those in other published works using smaller cells ( $0.04$  to  $0.1 \text{ cm}^2$ ), the performance of the champion cell was recorded with different apertures ranging from  $0.08$  to  $0.18 \text{ cm}^2$  (Figure S5). Device performances as a function of aperture size are summarized in Table S2. The slight variation in  $J_{\text{sc}}$  and/or  $V_{\text{oc}}$  with different aperture sizes may reflect inhomogeneity of the films at a microscopic scale. As expected, smaller cells showed increased performance, with up to 12.25% efficiency. Although our efficiencies are not among the best reported, notably, we were able to obtain high FFs (above 0.7) for more than half of the devices fabricated at a size of  $0.18 \text{ cm}^2$  (Figure S6).

Although substantial attention has been paid to achieving high efficiency, anomalous J-V hysteresis behavior has been not fully disclosed on many occasions in earlier reports. Device performance can depend markedly on voltage sweep rate or direction, or both. To investigate the hysteresis behavior of our  $\text{MAPbI}_{3-x}\text{Cl}_x$  devices, we measured their J-V characteristics at different scan rates from  $0.02$  to  $0.3 \text{ V s}^{-1}$  in the forward ( $-0.2$  to  $1.2 \text{ V}$ ) and reverse ( $1.2$  to  $-0.2 \text{ V}$ ) directions (Figure 6). The origin of hysteresis in perovskite-absorber devices has been assigned to the slow dynamic processes originating from the trapping and detrapping of charge carriers, as well as to changes in absorber or contact conductivity, ferroelectricity, and ion migration.<sup>17-20</sup> All of these effects appear to be related to the

structural quality of the perovskite layer. The absence of hysteresis in our devices suggests that the fabrication method presented here is good enough to prevent such anomalous behaviors in devices. To obtain more quantitative information on J-V hysteresis, we estimated a hysteresis index (HI) by using the equation<sup>19</sup>

$$\text{Hysteresis index} = \frac{J_{RS}(0.8 V_{oc}) - J_{FS}(0.8 V_{oc})}{J_{RS}(0.8 V_{oc})}$$

where  $J_{RS}(0.8 V_{oc})$  and  $J_{FS}(0.8 V_{oc})$  represent the photocurrent density at 80% of  $V_{oc}$  for the reverse scan (RS) and forward scan (FS), respectively. A histogram of 80 devices (Figure S7) revealed that one-third of our devices had HI values below 0.1; this was a far better result than in other reports. In fact, this degree of near-absence of hysteresis allowed us to quantitatively analyze the perovskite photovoltaic cells by using analytical models and impedance spectroscopy (IS).<sup>21</sup>

We further examined the photostability of our devices under illumination (1 sun) (Figure 7 (a)). Devices were operated alternately between short and open circuit conditions under continuous illumination. No degradation of the  $\text{MAPbI}_{3-x}\text{Cl}_x$  devices was found during 2 h of operation, revealing a high degree of stability. In contrast, the  $\text{MAPbI}_3$  devices showed a gradual decrease in  $J_{sc}$  in the same photostability testing. Similarly, higher stability for devices using  $\text{PbCl}_2$  as lead source, instead of non-Cl containing  $\text{Pb(OAc)}_2$ , has been reported,<sup>35</sup> which is another example of the positive effect gained by the inclusion of chlorine species. More interestingly (Figure S8), hysteresis-free J-V behavior lasted for more than 1 month in the case of  $\text{MAPbI}_{3-x}\text{Cl}_x$  devices, revealing the high degree of stability of perovskite solar cells prepared by using the Cl-doped interdiffusion method.

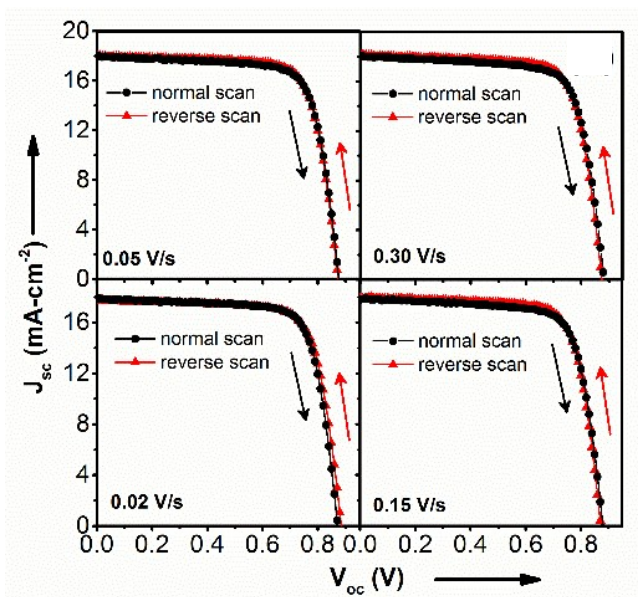


**Figure 6.** J-V curves of MAPbI<sub>3-x</sub>Cl<sub>x</sub> devices with different scan rates.

Halide perovskites can be very sensitive to moisture and easily decomposed because of the highly hygroscopic nature of the amine salts.<sup>36</sup> Therefore, the stability of perovskite photovoltaic devices is usually poor under ambient atmosphere, limiting the use of these devices in practical applications without encapsulation. We investigated the aging of our devices stored under ambient atmosphere by using a common method of encapsulation with cavity glass and UV-curable resin. The PCE of MAPbI<sub>3-x</sub>Cl<sub>x</sub> devices retained 90% of its initial value for almost 2 months in some cases (Figure 7(b)). Possible mechanisms behind the deterioration after 2 months are degradation at the PEDOT:PSS–perovskite interface as a result of the acidic or hygroscopic nature of PEDOT:PSS, or oxidation of the thin Ca layers at the cathode contact. Further optimization of interface materials will be needed to replace these materials and produce perovskite photovoltaic devices with practical durability.

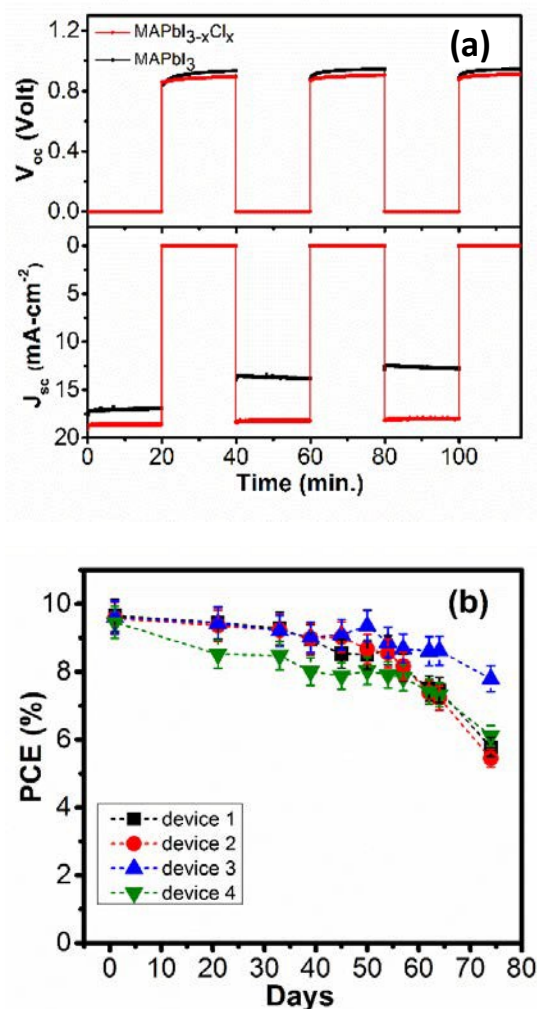


**Figure 7.** (a) Comparison of device performances under continuous illumination (1 sun). (b) Long-term stability of  $\text{MAPbICl}_{3-x}\text{Cl}_x$  devices stored under ambient atmosphere [device size  $0.18 \text{ cm}^2$ ].

In summary, we demonstrated low-temperature solution-processed perovskite photovoltaic devices with hysteresis-free J-V characteristics and excellent long-term stability. Our devices showed promising stability by maintaining more than 90% of their initial performance over 2 months at ambient conditions when we used a common method of encapsulation in cavity glass and UV-curable resin. We compared the photovoltaic properties and stabilities of two different lead-halide perovskite devices (i.e.  $\text{MAPbI}_3$  and  $\text{MAPbI}_{3-x}\text{Cl}_x$ ) fabricated (size  $0.18 \text{ cm}^2$ ) by using the interdiffusion method. Inclusion of chlorine in the interdiffusion method effectively enhanced the stability and reproducibility of the devices in comparison with those of  $\text{MAPbI}_3$  devices. The key factors that improved the performance of  $\text{MAPbI}_{3-x}\text{Cl}_x$  devices were better crystallinity and homogeneity and pin hole-free coverage of the perovskite films, as revealed by XRD and SEM observations. Further improvements in device performance are anticipated through rational interface engineering.

## Acknowledgement

The authors acknowledge the support under the MEXT Program for Development of Environmental Technology using Nanotechnology.

Supplementary Information (ESI) available: XPS data for MAPbI<sub>3</sub> and MAPbI<sub>3-x</sub>Cl<sub>x</sub>, SEM images for MAPbI<sub>3-x</sub>Cl<sub>x</sub>, and PbI<sub>2</sub>, FF histogram and hysteresis index values.

## REFERENCES

1. P. Gao, M. Gratzel and M. K. Nazeeruddin, *Energ Environ Sci*, 2014, **7**, 2448-2463.
2. A. Kojima, K. Teshima, Y. Shirai and T. Miyasaka, *J. Am. Chem. Soc.*, 2009, **131**, 6050-6051.
3. M. Z. Liu, M. B. Johnston and H. J. Snaith, *Nature*, 2013, **501**, 395-398.
4. J. Burschka, N. Pellet, S. J. Moon, R. Humphry-Baker, P. Gao, M. K. Nazeeruddin and M. Gratzel, *Nature*, 2013, **499**, 316-319.
5. Z. Xiao, C. Bi, Y. Shao, Q. Dong, Q. Wang, Y. Yuan, C. Wang, Y. Gao and J. Huang, *Energ Environ Sci*, 2014, **7**, 2619-2623.
6. J. H. Im, I. H. Jang, N. Pellet, M. Gratzel and N. G. Park, *Nature Nanotechnology*, 2014, **9**, 927-932.
7. H. Zhou, Q. Chen, G. Li, S. Luo, T.-b. Song, H.-S. Duan, Z. Hong, J. You, Y. Liu and Y. Yang, *Science*, 2014, **345**, 542-546.
8. Q. Lin, A. Armin, R. C. R. Nagiri, P. L. Burn and P. Meredith, *Nat Photon*, 2015, **9**, 106-112.
9. M. M. Lee, J. Teuscher, T. Miyasaka, T. N. Murakami and H. J. Snaith, *Science*, 2012, **338**, 643-647.
10. D. Y. Liu and T. L. Kelly, *Nature Photonics*, 2014, **8**, 133-138.
11. J.-H. Im, H.-S. Kim and N.-G. Park, *APL Mater.*, 2014, **2**, 081510.
12. J. Y. Jeng, Y. F. Chiang, M. H. Lee, S. R. Peng, T. F. Guo, P. Chen and T. C. Wen, *Adv. Mater.*, 2013, **25**, 3727-3732.
13. A. Abrusci, S. D. Stranks, P. Docampo, H. L. Yip, A. K. Y. Jen and H. J. Snaith, *Nano Lett.*, 2013, **13**, 3124-3128.
14. J. You, Z. Hong, Y. Yang, Q. Chen, M. Cai, T.-B. Song, C.-C. Chen, S. Lu, Y. Liu, H. Zhou and Y. Yang, *ACS Nano*, 2014, **8**, 1674-1680.
15. O. Malinkiewicz, A. Yella, Y. H. Lee, G. M. Espallargas, M. Graetzel, M. K. Nazeeruddin and H. J. Bolink, *Nature Photonics*, 2014, **8**, 128-132.
16. C.-H. Chiang, Z.-L. Tseng and C.-G. Wu, *Journal of Materials Chemistry A*, 2014, **2**, 15897-15903.
17. H. J. Snaith, A. Abate, J. M. Ball, G. E. Eperon, T. Leijtens, N. K. Noel, S. D. Stranks, J. T. W. Wang, K. Wojciechowski and W. Zhang, *J Phys Chem Lett*, 2014, **5**, 1511-1515.
18. R. S. Sanchez, V. Gonzalez-Pedro, J. W. Lee, N. G. Park, Y. S. Kang, I. Mora-Sero and J. Bisquert, *J Phys Chem Lett*, 2014, **5**, 2357-2363.
19. H. S. Kim and N. G. Park, *J Phys Chem Lett*, 2014, **5**, 2927-2934.
20. E. L. Unger, E. T. Hoke, C. D. Bailie, W. H. Nguyen, A. R. Bowring, T. Heumuller, M. G. Christoforo and M. D. McGehee, *Energ Environ Sci*, 2014, **7**, 3690-3698.
21. K. Miyano, M. Yanagida, N. Tripathi and Y. Shirai, *Appl. Phys. Lett.*, 2015.
22. E. L. Unger, A. R. Bowring, C. J. Tassone, V. L. Pool, A. Gold-Parker, R. Cheacharoen, K. H. Stone, E. T. Hoke, M. F. Toney and M. D. McGehee, *Chem. Mater.*, 2014, **26**, 7158-7165.

23. S. T. Williams, F. Zuo, C. C. Chueh, C. Y. Liao, P. W. Liang and A. K. Y. Jen, *ACS Nano*, 2014, **8**, 10640-10654.
24. M. I. Dar, N. Arora, P. Gao, S. Ahmad, M. Grätzel and M. K. Nazeeruddin, *Nano Lett.*, 2014, **14**, 6991-6996.
25. S. Colella, E. Mosconi, G. Pellegrino, A. Alberti, V. L. P. Guerra, S. Masi, A. Listorti, A. Rizzo, G. G. Condorelli, F. De Angelis and G. Gigli, *The Journal of Physical Chemistry Letters*, 2014, **5**, 3532-3538.
26. R. Steim, F. R. Kogler and C. J. Brabec, *J. Mater. Chem.*, 2010, **20**, 2499-2512.
27. M. Jiang, J. Wu, F. Lan, Q. Tao, D. Gao and G. Li, *Journal of Materials Chemistry A*, 2015, **3**, 963-967.
28. A. L. Patterson, *Physical Review*, 1939, **56**, 978-982.
29. Y. X. Zhao and K. Zhu, *J Phys Chem C*, 2014, **118**, 9412-9418.
30. E. Edri, S. Kirmayer, A. Henning, S. Mukhopadhyay, K. Gartsman, Y. Rosenwaks, G. Hodes and D. Cahen, *Nano Lett.*, 2014, **14**, 1000-1004.
31. J. M. Ball, M. M. Lee, A. Hey and H. J. Snaith, *Energ Environ Sci*, 2013, **6**, 1739-1743.
32. S. Colella, E. Mosconi, P. Fedeli, A. Listorti, F. Gazza, F. Orlandi, P. Ferro, T. Besagni, A. Rizzo, G. Calestani, G. Gigli, F. De Angelis and R. Mosca, *Chem. Mater.*, 2013, **25**, 4613-4618.
33. J. H. Noh, S. H. Im, J. H. Heo, T. N. Mandal and S. I. Seok, *Nano Lett.*, 2013, **13**, 1764-1769.
34. P. Docampo, F. C. Hanusch, S. D. Stranks, M. Doblinger, J. M. Feckl, M. Ehrensperger, N. K. Minar, M. B. Johnston, H. J. Snaith and T. Bein, *Advanced Energy Materials*, 2014, **4**, 6.
35. F. K. Aldibaja, L. Badia, E. Mas-Marza, R. S. Sanchez, E. M. Barea and I. Mora-Sero, *Journal of Materials Chemistry A*, 2015, **3**, 9194-9200.
36. B. Suarez, V. Gonzalez-Pedro, T. S. Ripolles, R. S. Sanchez, L. Otero and I. Mora-Sero, *J Phys Chem Lett*, 2014, **5**, 1628-1635.